



# A numerical approach to analyze the burrs generated in the drilling of carbon fiber reinforced polymers (CFRPs)

Fuji Wang<sup>1</sup> · Xiaonan Wang<sup>1</sup> · Xiang Zhao<sup>1</sup> · Guangjian Bi<sup>1</sup> · Rao Fu<sup>2</sup>

Received: 4 May 2019 / Accepted: 19 December 2019 / Published online: 6 January 2020  
© Springer-Verlag London Ltd., part of Springer Nature 2020

## Abstract

Burrs generated in the drilling process of carbon fiber-reinforced polymers (CFRPs) can cause delamination, therefore significantly reduce the bearing capacity of the components during service. In order to address this issue, the multiscale finite element (FE) modeling was developed in this work to analyze the burrs formation mechanism. The proposed model combined the microscopic fiber and matrix phases with the macroscopic equivalent homogeneous material (EHM). Meanwhile, 3D Hashin-type damage initiation criteria were proposed to characterize the differences between the tensile and compressive strength of the EHM and fiber and their anisotropy feature. The cutting of the fiber and matrix phases under all cutting angles were divided into two simulation processes to improve the computational efficiency. With the help of this model, the thrust force was accurately predicted where the distribution of burrs was successfully simulated compared with the experimental measurements. In addition, the evolution process from the failure of the fiber and matrix phases towards formation of the burrs was clarified. It could be seen that in the drilling of the CFRPs at the hole exit, the matrix was removed while the fibers deformed out-of-plane under the push of the drill firstly rather than got removed and then bent with the rotation of the drill. Specifically, the fibers under acute cutting angles bent outward the hole radially, which made them more difficult to be removed and hence resulted in the burrs eventually. The revealed formation mechanisms would be the crucial contribution and guidance for helping to suppress the burrs.

**Keywords** CFRPs · Drilling · Burrs · Finite element modeling · Multiscale simulation · Cutting angle · Formation mechanism

## 1 Introduction

Carbon fiber-reinforced polymers (CFRPs) exhibit extraordinary mechanical properties such as high specific strength, high specific modulus, and excellent impact and fatigue resistance. These properties make them a favorable material in aerospace, transportation, and energy sectors where the requirement of lightweight for the structural components is always priority [1–8]. In assembly of CFRP components, the drilling process is usually operated for joining purpose [9–11] and therefore the high standard quality holes are crucial to ensure the safe and reliable performance. However, CFRP is one of the typical difficult-to-cut material [12]. The difference in mechanical properties of the

material composition results in a very unique cutting performance of the CFRPs, e.g., the fiber is difficult to cut due to high strength, whereas the matrix is relatively easier to be failed and completely removed [3, 13–15]. In this situation, the serious damages such as burr, fiber-matrix debonding, fiber pull-out, and delamination are difficult to avoid during the drilling of CFRPs [2, 16–21]. Such damages could significantly reduce the load-bearing capacity and shorten the service life of the components [22–24]. Therefore, it is a main task for composite engineers to minimize or vanish these drilling damages based on the full understanding of the damage initiation and growth mechanisms.

However, due to drilling is a rapid processing, the drilling induced damage is rarely capable to be observed through the experimental approach. It is time and cost consuming while the cutting chips of CFRPs are harmful to experimenters [25–27]. Moreover, although great efforts based on high-speed [28, 29] or thermal camera [30] have been recently reported to measure the drilling damage formation, the observations are still not clear enough and the cutting conditions of inside layers are barely visible and identified. Therefore, finite

✉ Fuji Wang  
wfjsll@dlut.edu.cn

<sup>1</sup> School of Mechanical Engineering, Dalian University of Technology, Dalian 116024, China

<sup>2</sup> School of Mechanical and Aerospace Engineering, Queen's University Belfast, Belfast BT9 5AG, UK

element (FE) simulation is a cost-saving method to analyze the multi-damage modes and their interactions within the CFRPs during drilling. With an accurate model, it is reliable to figure out the drilling process at different scales and positions and analyze the various damages produced within the composite laminates. FE model is thus helpful to explain the complicated damage initiation and evolution, but also avoiding the influences of experimental conditions (e.g., tool wear and material inherent defects) on the results [31, 32]. Therefore, FE simulation is preferred to study the formation mechanisms of the damages due to drill the CFRPs.

It could be found the most CFRP drilling simulation focused on the study of the delamination. Isbilir et al. [33, 34] developed a 3D FE model based on the theory of Hashin and the cohesive element and studied the effects of stage ratios of step drill on delamination. Phadnis et al. [35, 36] researched the effects of drilling parameters on the initiation and propagation of delamination by simulation. Feito et al. [37, 38] studied the influences of thrust force, stacking sequence, and tool geometry on delamination through the CFRP drilling simulation. However, the burrs, which is another main damage mode occurred during drilling process, have been rarely reported. Missing such damage by the FE modeling would fail to accurately predict the mechanical behavior of drilled composite as the burrs might accelerate the delamination initiation and propagation, and fiber pull-out under the continuous scratch of the cutting tool edges. Meanwhile, although burrs could be removed by post process, it will increase the circle time. Therefore, the formation mechanism of burrs should be figured out to help the improvement of the drilling quality and efficiency.

In recent years, most FE models for the simulation of CFRP drilling were developed based on the equivalent homogeneous material (EHM) assumption where the individual layer of the composite laminate was defined to be equivalently homogeneous [33–39]. However, it has to be pointed out the burr formation process is related to the local removal of fibers and matrix at the microscopic level. EHM without consideration of the effects of cutting tool on fibers and matrix is obviously no longer appropriate for the investigation on the burrs [40]. In this case, a FE model involving both fiber and matrix phases has become a main challenge to study the burrs induced by drilling process. Considering that the fiber and matrix have drastically different mechanical properties and complex interactions existed between these two phases during drilling, different constitutive laws as well as damage initiation and evolution criteria need to be specifically defined to reflect their material behaviors. In particular, more attention should be paid to the anisotropy behavior and difference between tensile and compressive strengths of the fibers, as well as their damage accumulation prior to failure [41–44].

Besides, another main obstacle for the CFRP drilling simulation is the extremely low calculating efficiency. Although the computing power has advanced greatly in recent years, the

simulation of the CFRP drilling still takes a very long time. In fact, the element quantity and mesh size of the model have great effects on the computational efficiency [45]. An increase in the element quantity or a decrease in the mesh size will result in an exponential increase in simulation time. That means, if the model is developed only at the microscopic level and the workpiece consists entirely of fiber and matrix phases, the model will be too fine and the simulation time will be unlimited, which will result in the failure of the analysis of the burr. Therefore, it is necessary to develop effective methods to improve the computational efficiency.

In this paper, a three-dimensional FE model with multiscale modeling was proposed and applied for the first time to analyze the formation mechanism of the burrs generated during the drilling of CFRPs. The proposed FE model combined both the microscopic fiber and matrix phases and the macroscopic EHM together, with the specific damage initiation criteria and damage evolution laws to reflect their material behaviors. In particular, strain-based three-dimensional Hashin-type damage initiation criteria were proposed to characterize the anisotropy and difference between tensile and compressive strength of the EHM and fiber phase while the exponential continuum damage mechanics based evolution laws were applied to model the damage growth until complete failure. In addition, several methods were developed to improve the computational efficiency, such as dividing the cutting of fiber and matrix phases under different cutting angles into two simulation processes for parallel computation and optimizing the geometrical distribution of the EHM as well as the fiber and matrix phases. Then, the experimental measurements of drilling of composites were performed to validate the FE model developed in this work to help identify the reliability of the proposed FE model. Through the analysis of the simulation results, the evolution process from the failure of the fiber and matrix phases to the burr formation was obtained, and the burr formation mechanism was revealed. Finally, the computational efficiency of this model and the possible solutions for suppressing burrs were discussed.

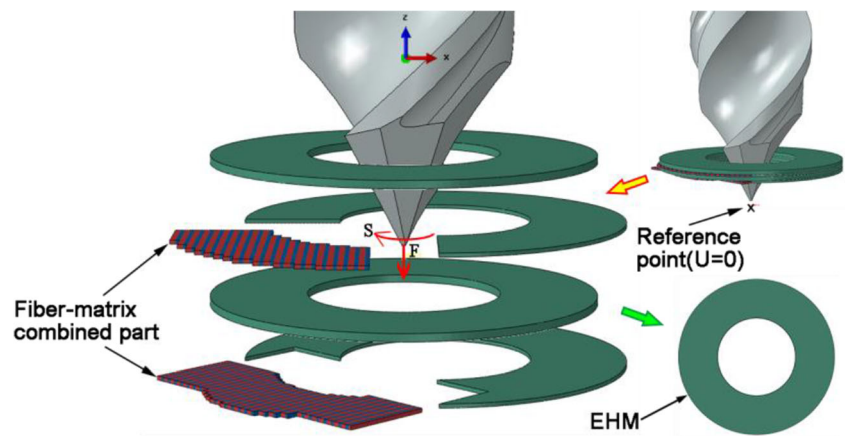
## 2 Finite element modeling

For the study, the main challenge is to successfully predict the burrs, a FE model was therefore initially developed to simulate the drilling based on the combination of multiscale CFRPs simulation. The geometry and elements, boundary conditions, and material behaviors of the model are specified in details by this section.

### 2.1 Geometrical model

The model was developed using the commercial software Abaqus/Explicit. Dynamic explicit analysis was selected due

Fig. 1 Details of the geometrical model



to the complex contact between the drill and the workpiece during drilling. Details of the geometrical model are shown in Fig. 1.

### 2.1.1 Geometry and elements of the drill bit and composite workpiece

Twist drill bit with a diameter of 4 mm and a point angle of 90° was modeled in the commercial modeling software UG and then imported into the Abaqus. 4-node linear tetrahedron elements without element deletion (C3D4 [46]) were defined for the drill bit.

In order to improve the computational efficiency of the model under a reliable accuracy, several strategies were developed for the geometric model of the workpiece. Firstly, the outer diameter of the workpiece was set about 6 mm, and the workpiece was simplified to two plies with different fiber orientations. These two plies were defined as top layer and bottom layer according to the processing sequence. Secondly, a pre-drilled hole was set in the laminates to minimize the quantity of integration points involved in the computation. Thirdly, a multiscale modeling was applied in the simulation. As illustrated by Fig. 1, a fiber-matrix combined part that consists of fiber and matrix phases was defined in the bottom of each layer of the laminate, and the other part of the workpiece was assumed to be EHM. The meshes in the fiber-matrix combined part were particularly refined to accurately describe the effects of the tool onto the fiber and matrix phases while the relatively coarse meshes were given in the EHM area to

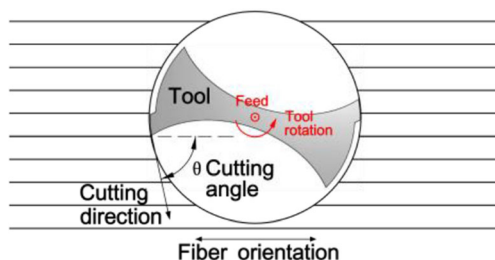


Fig. 2 A schematic of definition of the cutting angle in the CFRP drilling

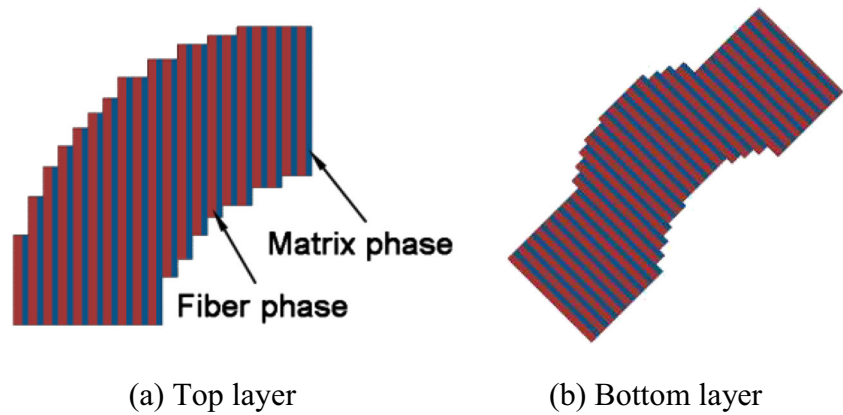
improve the computational efficiency [47]. Last but not least, the cutting of fiber and matrix phases under different cutting angles were divided into two simulation processes named simulation-I and simulation-II for parallel computation, and the geometrical distribution of both the EHM and the fiber and matrix phases in these two simulations was optimized as described below. In this paper, the cutting angle is defined from the bottom view of the workpiece, and measured counterclockwise from the cutting direction of the cutting edge to the fiber orientation, as seen in Fig. 2. In this case, according to the fiber orientations illustrated in Fig. 3, the cutting angle of the fiber-matrix combined part in the top layer covered from 0° to 90° where the bottom layer covered from 45° to 135° in simulation-I. Simultaneously, in simulation-II, the fiber orientations were changed, and the cutting angle of the fiber-matrix combined part in the top layer covered from 90° to 180° and in the bottom layer covered from 0° to 45° and 135° to 180° (shown in Fig. 4). With the help of these two simulations, the interactions between the tool and the fiber and matrix phases in each layer at all cutting angles were studied. The cutting angles for the fiber-matrix combined part in different simulations and different layers are listed in Table 1.

The workpiece was defined by the 8-node linear brick element with reduced integration (C3D8R [46]) method [34, 36-38]. However, since the reduced integration elements use the lower-order integration to form the element stiffness, the hourglassing problem occurs frequently during the simulation. This problem would result in large distortions of the elements and therefore have to reduce the time increment of the procedure, eventually greatly extend the computational time and even terminate the simulation. Therefore, the enhanced hourglass control approach was used to minimize the hourglassing:

$$Q = sKq \tag{1}$$

where  $Q$  is the resistance force,  $s$  is the scaling factor,  $K$  is the linear stiffness, and  $q$  is the hourglass mode magnitude. In addition, the distortion control was used to control the element distortion. The aspect ratio of the meshes around the drill was

**Fig. 3** The fiber-matrix combined part in simulation-I: **a** top layer, **b** bottom layer



set as one to ensure that the meshes would not distort during the calculation, and that away from the drill was set about two to reduce the computational time.

### 2.1.2 Boundary conditions and interactions

The rotational and translational velocities in  $Z$  direction were applied to the drill body as spindle speed and feed rate, respectively. The feed rate and spindle speed adopted commonly used values, which are 150 mm/min and 3000 rpm, respectively [36, 48]. Meanwhile, all nodes on the outer diameter of the laminates were coupled with a reference point through the kinematic coupling, and all degrees of freedom of the reference point were limited to prevent the workpiece from moving.

Surface-to-surface kinematic contact algorithm was used to simulate the interactions between the tool and workpiece [34, 49]. The contact forces were calculated based on the penalty contact method, and the friction coefficient was set as 0.3 based on the previous study [50]. Meanwhile, in order to avoid penetration, a general contact was defined between each ply of the workpiece.

### 2.2 Material modeling

In this model, the deformation and abrasion of the tool were not considered and it was assumed to be rigid body. The density and elastic modulus of the drill were defined, while the damage initiation criteria and damage evolution laws were not.

For the workpiece, its material was defined via material modeling of both the EHM and fiber and matrix phases. In most recent researches reported on the drilling simulation of CFRPs, a degradation parameter was most popular way to express the damage growth until complete failure [36–38]. This approach would result in missing the progressive damage evolution. In addition, fibers in orthogonal cutting simulation models were usually assumed to be brittle, and the difference between tensile and compressive strength and the damage accumulation was not considered [51–54], which could further affect the accuracy of the damage prediction. In this research, the material behavior of the EHM and fiber phase represented by the typical anisotropy and difference between tensile and compressive strength as well as damage accumulation were considered. The material behavior of the matrix phase was assumed to be isotropic.

**Fig. 4** The fiber-matrix combined part in simulation-II: **a** top layer, **b** bottom layer

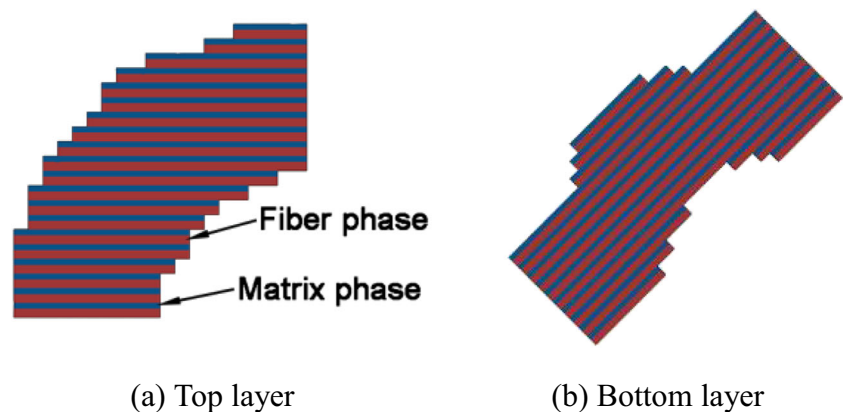


**Table 1** Cutting angles in different simulations and different layers

Layer	Simulation-I	Simulation-II
Top layer	0°-90°	90°-180°
Bottom layer	45°-135°	0°-45° and 135°-180°

**2.2.1 Material behavior of the EHM and fiber phase**

Considering the orthotropic material properties of the fiber phase and EHM, their material behavior in the longitudinal direction (direction 1), transverse direction (direction 2) and through-thickness direction (direction 3) were defined. Linear elastic material behavior was applied to them until failure:

$$\sigma_i = C_{ij} \varepsilon_j \tag{2}$$

The damage initiation criteria including different failure modes were developed based on the theory of Hashin. When implementing the stress-based Hashin criteria, the dramatically varying stresses due to the degradation of material properties may cause numerical instability. To solve this problem, Yang et al. [55] applied strain-based Hashin criteria. However, the criteria they used contain the failure of the materials in longitudinal and transverse directions except for that in through-thickness direction. Therefore, new damage initiation criteria were proposed in this paper, and the material failure in the through-thickness direction was considered to characterize the intralaminar failure of the CFRP. The damage initiation criteria are shown in Table 2. When the failure index  $F$  reaches one, the corresponding mode of failure initiates and the damage occurs.

Subscripts  $f$ ,  $m$ , and  $d$  in Table 2 denote the longitudinal, transverse, and through-thickness directions, respectively, the subscript  $t$  and  $c$  stand for tensile and compressive failure respectively,  $\varepsilon$  and  $\gamma$  are the normal strain and shear strain,

and the term with a superscript  $f$  is the corresponding failure strain. The failure strains  $\varepsilon_{1t}^f, \varepsilon_{1c}^f, \varepsilon_{2t}^f, \varepsilon_{2c}^f$ , and  $\gamma_{ij}^f$  can be calculated according to the previous study [55]. Moreover, the tensile failure strain in the through-thickness direction can be obtained from the following equation.

$$\varepsilon_{3t}^f = Z_t / E_3 \tag{3}$$

Wherein  $Z_t$  and  $E_3$  are the tensile strength and the elastic modulus in the through-thickness direction respectively.

If damage is detected, the element stiffness begins to degrade according to the exponential damage evolution laws, as shown in Fig. 5. That is, when the damage initiation criterion is satisfied (point B), the damage variable  $d$  in the corresponding direction starts to increase according to Eq. (4) from zero. When  $d$  reaches one, the stiffness of the element degrades to zero and the material fails completely.

$$\begin{aligned} d_{fi} &= 1 - e^{-X_i \varepsilon_{it}^f (F_{fi} - 1)^{L^c} / G_{fi} / F_{fi}} \\ d_{mi} &= 1 - e^{-Y_i \varepsilon_{it}^f (F_{mi} - 1)^{L^c} / G_{mi} / F_{mi}} \\ d_{di} &= 1 - e^{-Z_i \varepsilon_{it}^f (F_{di} - 1)^{L^c} / G_{di} / F_{di}} \end{aligned} \tag{4}$$

In Eq. (4),  $L^c$  is the characteristic length of the element,  $G_{fi}$ ,  $G_{mi}$ , and  $G_{di}$  are the fracture energies corresponding to the failure in the longitudinal, transversal, and through-thickness directions, and  $i$  equals  $t$  or  $c$  representing tensile or compressive failure respectively. The fracture energy and characteristic length were introduced into the applied damage evolution laws to guarantee the damage evolutions are progressive and reduce the mesh dependence of the simulation results.

The material behavior of the EHM and fiber phase was implemented into Abaqus/Explicit through a user-defined subroutine (VUMAT), and the element deletion during the simulation was controlled by a state variable defined in the VUMAT. The material properties of the EHM and fiber phase

**Table 2** The strain-based 3D damage initiation criteria

Failure mode	Failure criterion
Tensile failure in the longitudinal direction	$F_{fi}^2 = \left(\frac{\varepsilon_1}{\varepsilon_{1t}^f}\right)^2 + \left(\frac{\gamma_{12}}{\gamma_{12}^f}\right)^2 + \left(\frac{\gamma_{13}}{\gamma_{13}^f}\right)^2$
Compressive failure in the longitudinal direction	$F_{fc}^2 = \left(\frac{\varepsilon_1}{\varepsilon_{1c}^f}\right)^2$
Tensile failure in the transverse direction	$F_{mt}^2 = \left(\frac{\varepsilon_2 + \varepsilon_3}{\varepsilon_{2t}^f}\right)^2 - \frac{\varepsilon_2 \varepsilon_3}{(\gamma_{23}^f)^2} + \left(\frac{\gamma_{12}}{\gamma_{12}^f}\right)^2 + \left(\frac{\gamma_{13}}{\gamma_{13}^f}\right)^2 + \left(\frac{\gamma_{23}}{\gamma_{23}^f}\right)^2$
Compressive failure in the transverse direction	$F_{mc}^2 = \left(\frac{\varepsilon_2 + \varepsilon_3}{\varepsilon_{2c}^f}\right)^2 \left[ \left(\frac{\varepsilon_{2t}^f}{2\gamma_{23}^f}\right)^2 - 1 \right] + \left(\frac{1}{2\gamma_{23}^f}\right) (\varepsilon_2 + \varepsilon_3)^2 + \left(\frac{1}{\gamma_{23}^f}\right) (\gamma_{23}^2 - \varepsilon_{22} \varepsilon_{33}) + \left(\frac{\gamma_{12}}{\gamma_{12}^f}\right)^2 + \left(\frac{\gamma_{13}}{\gamma_{13}^f}\right)^2 + \left(\frac{\gamma_{23}}{\gamma_{23}^f}\right)^2$
Tensile failure in the through-thickness direction	$F_{dt}^2 = \left(\frac{\varepsilon_3}{\varepsilon_{3t}^f}\right)^2 + \left(\frac{\gamma_{13}}{\gamma_{13}^f}\right)^2 + \left(\frac{\gamma_{23}}{\gamma_{23}^f}\right)^2$
Compressive failure in the through-thickness direction	$F_{dc}^2 = \left(\frac{\gamma_{13}}{\gamma_{13}^f}\right)^2 + \left(\frac{\gamma_{23}}{\gamma_{23}^f}\right)^2$

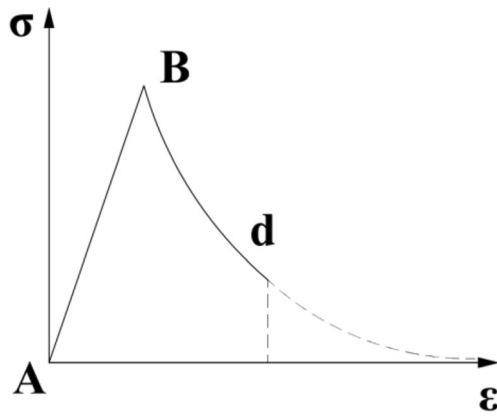


Fig. 5 Material behavior of the EHM and fiber phase

obtained through consulting manufacturers and referring to [56] are shown in Table 3, in which  $\nu_{ij}$  is the Poisson’s ratio and  $\rho$  is the density.

### 2.2.2 Material behavior of the matrix phase

In this research, elasto-plastic material behavior was assigned to the matrix until failure, and isotropic plastic hardening was used as shown in Fig. 6. The material properties of the matrix are shown in Table 3.

The damage initiation criterion used for the matrix is the shear damage criterion:

$$\omega_S = \int \frac{d\bar{\epsilon}^{pl}}{\bar{\epsilon}_S^{pl}(\theta_S, \bar{\epsilon}^{pl})} = 1 \tag{5}$$

Table 3 Material properties of the EHM and the fiber and matrix phases [56]

Material	Properties
EHM	$\rho = 1.53(\text{g}/\text{cm}^3)$
	$E_1 = 178(\text{GPa}), E_2 = E_3 = 9.5(\text{GPa})$
	$G_{12} = G_{13} = 6.33(\text{GPa}), G_{23} = 4.21(\text{GPa})$
	$\nu_{12} = \nu_{13} = 0.29, \nu_{23} = 0.37$
	$X_T = 2980(\text{MPa}), X_C = 1450(\text{MPa})$
Fiber	$\rho = 1.8(\text{g}/\text{cm}^3)$
	$E_1 = 294(\text{GPa}), E_2 = E_3 = 15(\text{GPa})$
	$G_{12} = G_{13} = 103(\text{GPa}), G_{23} = 89(\text{GPa})$
	$\nu_{12} = \nu_{13} = 0.25, \nu_{23} = 0.28$
	$X_T = 5880(\text{MPa}), X_C = 3850(\text{MPa})$
Matrix	$\rho = 0.98(\text{g}/\text{cm}^3)$
	$E = 3.4(\text{GPa})$
	$\nu = 0.4$
	$\sigma_{y0} = 85(\text{MPa})$

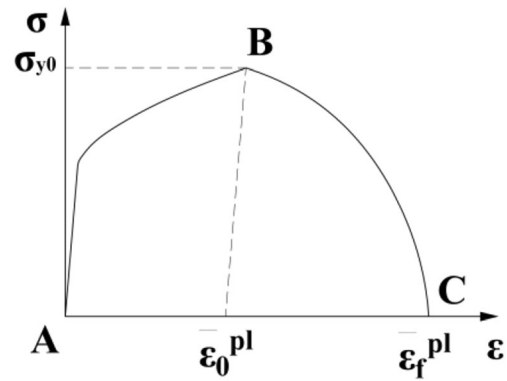


Fig. 6 Material behavior of the matrix phase

Once the damage initiation criterion is met, the damage variable  $d$  increases according to Eq. (6). The model ensures that the energy dissipation during the damage evolution process is equal to the fracture energy per unit area.

$$\dot{d} = \frac{L^c \dot{\bar{\epsilon}}^{pl}}{\bar{u}_f^{pl}} = \frac{\dot{\bar{u}}^{pl}}{\bar{u}_f^{pl}} \tag{6}$$

Wherein the equivalent plastic displacement at failure  $\bar{u}_f^{pl}$  is computed as

$$\bar{u}_f^{pl} = \frac{2G_f}{\sigma_{y0}} \tag{7}$$

$\sigma_{y0}$  is the stress at the time when the failure criterion is reached and  $G_f$  is the fracture energy per unit area.

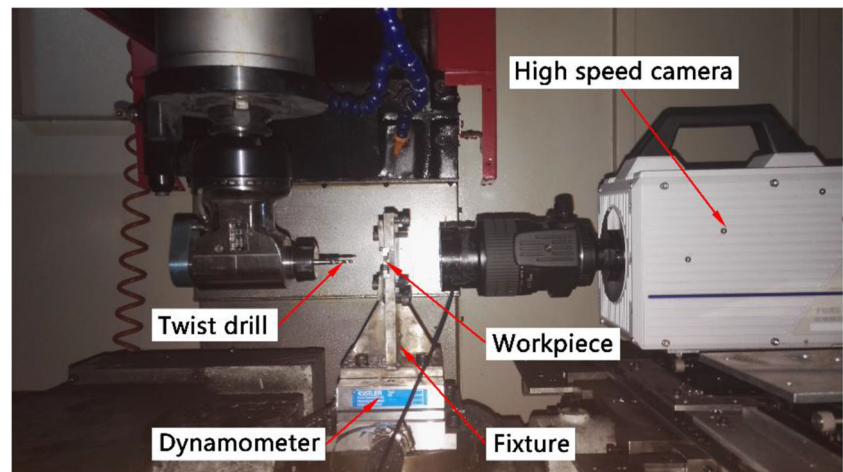
## 3 Experimental work

For the validation of the simulation, drilling experiments were performed in this study. Details of the drill bit and CFRPs, processing parameters, etc. were determined entirely based on the simulation. According to the workpiece in the FE model, pre-drilled holes were set in the laminates during the experiments. Meanwhile, the experiments were repeated to reduce the impact of experimental errors.

### 3.1 Experimental setup

Figure 7 shows the experimental setup. The CFRP drilling experiments were carried out on a GONA 5-axis machine center with the maximum spindle speed of 8000 rpm. A Kistler 9257B three-component dynamometer was used to record the cutting forces. A PHOTRON SA5 high-speed camera helped to record the drilling process at the hole exit. A KEYENCE VH-Z50L microscope helped to photograph the induced damage. The workpiece was clamped to the dynamometer through a designed fixture and the dynamometer

**Fig. 7** Setup of the drilling experiment



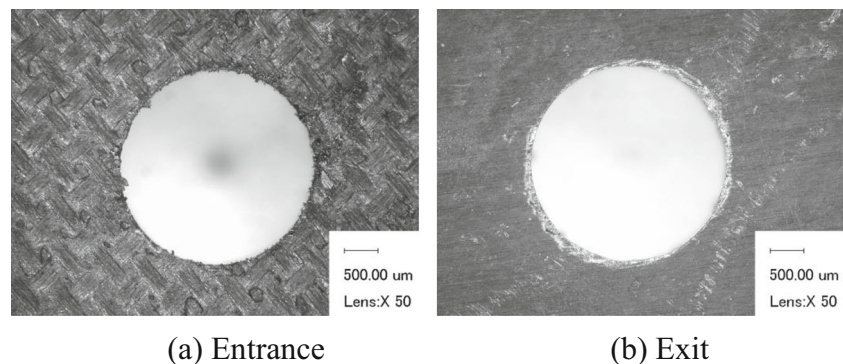
was fixed to ensure the drilling is stable enough. Since the support for the hole exit would affect the quality of the drilled holes, the fixture has a 14 mm diameter pre-drilled hole below the machining position of the workpiece, which helped to eliminate unnecessary influences.

In this research, the workpiece was manufactured by prepregs with the layout of  $[(-45/90/45/0)_2/90/90/90/90/90/(-45/90/45/0)_2]$ . The dimension of the workpiece is 150 mm  $\times$  20 mm  $\times$  4 mm to ensure that the workpiece can be placed in the fixture. Besides, the tool is made of YG8 cemented carbide.

### 3.2 The pre-drilled hole

During the experiments, 3-mm diameter pre-drilled holes were set in the workpiece firstly. Then, twist drills with a diameter of 4 mm were used to expand the pre-drilled holes so as to obtain the results used for the verification of the simulation. Figure 8 illustrates the entrance and exit of the pre-drilled hole. It is shown that there are little damage and no burr. The well-processed pre-drilled holes ensure that the initial states of the cutting area in the experiments are consistent with those in the FE model.

**Fig. 8** The pre-drilled hole: **a** entrance, **b** exit



(a) Entrance

(b) Exit

## 4 Simulation validation and results discussion

In this research, the CFRP drilling at 150 mm/min feed rate and 3000-rpm spindle speed was simulated. Through the simulation-I and simulation-II, the thrust force and the distribution of burrs were obtained. The simulation results were verified via the comparison with the experimental results. After that, the formation mechanism of the burrs was revealed via the analysis of the drilling process. Besides, computational efficiency of the FE model was discussed.

### 4.1 The thrust force

Since the thickness of the workpiece in FE model and experiment are 0.36 mm and 4 mm respectively, the complete time domain curves of the thrust force obtained by simulations and experiments could not be compared directly. However, in the early stage of the drilling, the machining status of the simulations is the same with the experiments. So, the thrust forces obtained in this period can be used for validation. Specifically, it is the period that starts from the beginning of the drilling to 0.17 s.

The filtered thrust forces from 0 to 0.17 s are shown in Fig. 9. It is indicated that the thrust forces increase with the feed of the tool, and the reason can be explained as follows. In this

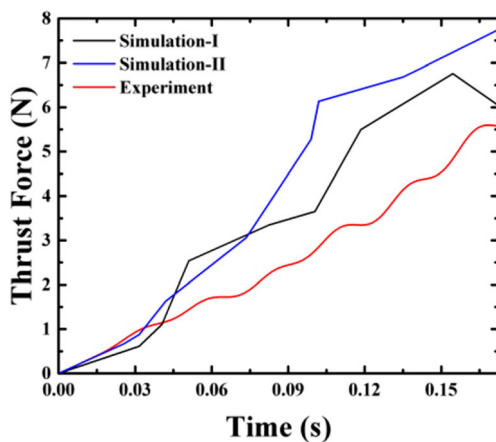


Fig. 9 The filtered thrust forces in the early stage of the drilling

period, the cutting area in the plane that perpendicular to the axis of the drill bit increases with the feed of the tool. The cutting depth of each cutting edge of the drill bit also increases with the increases of the cutting area, which in turn leads to an increase in cutting force. Since the point angle of the drill bit is constant during the drilling process, the cutting force component in the axial direction of the drill bit increases, which results in an increase in the thrust force.

To evaluate the error of the simulation results quantitatively, the growth rates of the thrust forces obtained by simulation-I, simulation-II, and experiments were compared, which are 39 N/s, 43 N/s, and 34 N/s, respectively, and the deviations between simulations and experiments are 13% and 21%, respectively. Therefore, the simulation forces are in acceptable agreement with the experimental forces. The cause of the error can be explained by the differences in the boundary conditions and drill bit between the simulations and experiments. In the FE model, the outer diameter of the workpiece is about 6 mm and all nodes on the outer diameter were fixed, and the drill bit was assumed to be rigid body. While in the experiment, the workpiece was fixed by a fixture with a pre-drilled hole. Meanwhile, the diameter of the drill bit is only 4 mm and its stiffness is comparatively low. Therefore, the workpiece and the drill bit were more likely to deform during the

experiments. Large deformation caused by thrust force would result in the decrease of the cutting depth of each cutting edge, and lead to the decrease of the thrust force in experiments. Thus, deviations were induced between the numerical and experimental forces.

## 4.2 Distribution of the formed burrs

In the FE model, the fiber-matrix combined part in the top layer is located away from the hole entrance and exit and that in the bottom layer is near the hole exit. Therefore, the burrs generated in the top layer were used to predict the burrs generated at the hole wall, while that generated in the bottom layer were used to predict the burrs generated at the hole exit. In the experiments, the generated burrs at the hole exit were measured from the bottom view of the hole. While considering that a vertical observation of the hole wall would destroy the processed holes, the top view of the hole was observed to measure the generated burrs at the hole wall.

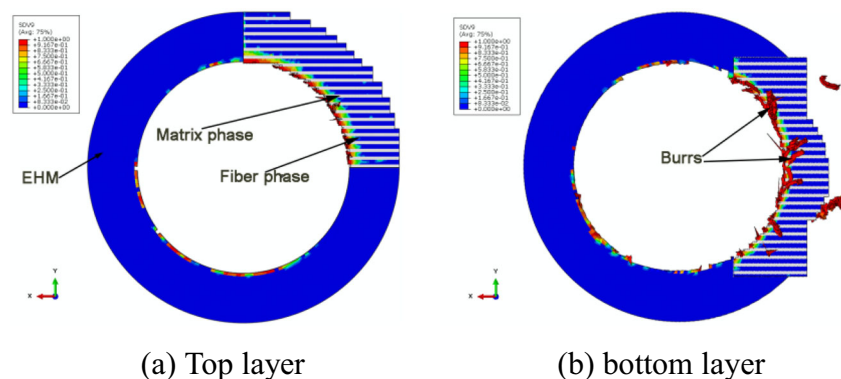
Meanwhile, in order to analyze the burrs quantitatively, the burr factor  $k = A_{\text{burr}}/A_{\text{hole}}$  was used to assess the burrs. Specifically, the burr factors for the simulations and experiments were defined as:

$$k_s^I = b \cdot \sum_{i=1}^n L_i^I/A; k_s^{II} = b \cdot \sum_{i=1}^n L_i^{II}/A; k_e = \sum_{i=1}^n A_i/A \quad (8)$$

where  $k_s^I$ ,  $k_s^{II}$ , and  $k_e$  are burr factors for simulation-I, simulation-II, and experiments, respectively;  $b$  is the width of the burrs in the simulations;  $\sum_{i=1}^n L_i^I$  and  $\sum_{i=1}^n L_i^{II}$  are the length sum of the burrs acquired by simulation-I and simulation-II, respectively;  $A$  is the area of the final hole. Since the width of the burrs is not constant in the experimental results, the area of them  $\sum_{i=1}^n A_i$  was adopted.

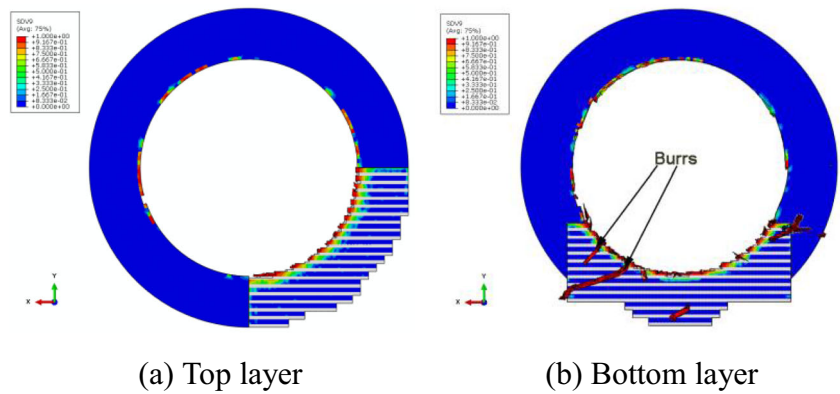
The burrs acquired by simulations and experiments are shown in Figs. 10, 11, and 12. To be specific, Figs. 10a, 11a, and 12a illustrate the burrs generated at the hole wall while the burrs generated at the hole exit are explained by Figs. 10b,

Fig. 10 Details of the drilled hole obtained by simulation-I: **a** top layer, **b** bottom layer





**Fig. 11** Details of the drilled hole obtained by simulation-II: **a** top layer, **b** bottom layer



11b, and 12b. It should be noted that, in the figures obtained by simulation-I and simulation-II, the blue area and white area in the fiber-matrix combined part symbolize the fiber and matrix phases, respectively, and the red area represents damage induced by drilling. The burr factors for the hole wall and exit are listed in Table 4.

From the simulation results, it can be seen that a lot of burrs were generated at the hole exit, while there is almost no burr at the hole wall. The results are consistent with those of the experimental measurements. The difference in the burr distribution between the hole exit and the wall could be explained by the change of the constraints. During the drilling of the CFRP components, there is no support below the material at the hole exit. Therefore, it is prone to out-of-plane deformation under the push of the drill. Once the deformation occurs, the material is hard to remove, which consequently results in the generation of the burrs. However, the material at the hole wall is supported by the material below, which weakens the out-of-plane deformation. Therefore, there is no burr around the hole wall.

For the hole exit, the distribution of the burrs obtained by simulations and experiments are illustrated in Fig. 13. Wherein, the black arrow shows the rotating direction of the tool. As mentioned before, the cutting angle for the fiber-matrix combined part in the bottom layer covers from 45° to 135° in simulation-I, and from 0° to 45° and 135° to 180° in simulation-II. Therefore, the distribution of the burrs at

different cutting angles can be acquired from Fig. 13 a and b, and the burr factors are listed in Table 5. It can be concluded that the burrs form easily when the cutting angle is acute, while there are few burrs when the cutting angle is obtuse. This result is consistent with the experimental result shown in Fig. 13 c. The difference in the burr distribution at different cutting angles can be explained as: when the cutting angle is acute, the fibers are relatively easier to bend outward the hole radially under the push of the cutting edges. In this case, the cutting force on the fibers has been reduced and the burrs are thus easily formed. While the cutting angle is obtuse, the fibers are prone to bend inward the hole radially. In this case, the stress of the fibers around the contact region has quickly exceeded the ultimate strength of the fiber and the burrs are rarely formed.

### 4.3 Analysis of the burrs formation mechanism

In this research, the drilling process at the hole exit was divided into four stages based on the interactions between the cutting edges of the tool and the last ply of the CFRPs, as shown in Fig. 14. Stage A was the period that the primary cutting edges started to cut the last ply. In Stage B, the removal of the last ply was conducted by the most part of the primary cutting edges. Following that, in Stage C, the minor cutting edges involved in the cutting of the last ply. With the feed of the drill, the hole was finished in Stage D. The four stages of the

**Fig. 12** Details of the drilled hole obtained by experiment: **a** top view, **b** bottom view

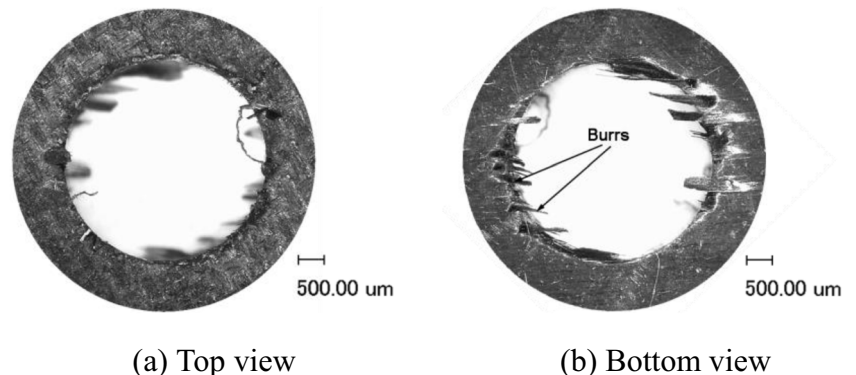


**Table 4** Burr factors at the hole wall and hole exit

	Hole wall	Hole exit
Simulation ( $k_s^I + k_s^{II}$ )	0	11.5%
Experiment	0	15.8%

drilling process at the hole exit were compared by the numerical modeling and experimental measurements.

Figure 15 illustrates the hole exit in Stage A. The numerical simulations have demonstrated part of the matrix phase was removed under the cutting of the primary cutting edges and the pressing of the flank faces. The fibers were forced to deform out-of-plane and spread out. For the experiments, the material was deformed under the push of the drill, and split into the strips under the squeeze of the drill while part of the material was removed.

In Stage B, as shown in Fig. 16, the cutting area around the hole exit was increased with the feed of the tool. For the simulations, almost all the matrix phase has been removed whereas the fibers were kept well due to the out-of-plane deformation. The fibers in the cutting area were bent with the rotation of the drill, and the bending direction was consistent with the rotation direction of the drill. The length of the remained fibers (i.e., the distance from the drilling edges to the free end of the fibers) became longer. In this case, the burrs were initiated. In the experiments, the tearing of the material was propagated along the direction of the fibers under the action of the drill, which resulted in the increase of the length of the strip-like material. Similarly, the material was bent to the rotation direction with the drill.

In Stage C, as seen from the simulations, the fibers marked in Fig. 17 a and b (i.e., the area where the cutting angle is obtuse) were effectively removed without inducing burrs or delamination. However, the rest of the fibers were remained due to bending. The experimental results showed that the material marked in Fig. 17 c was completely removed and the machined-surface was in a great condition. However, a large amount of strip-like material was found in the rest of the circumference of the hole.

**Table 5** Distribution of the burrs at different cutting angles

	Cutting angle	Burr factor
Simulation	0°-45° (simulation-II), 45°-90° (simulation-I)	9.5%
	90°-135° (simulation-I), 135°-180° (simulation-II)	2.0%
Experiment	0°-90°	12.9%
	90°-180°	2.9%

In Stage D, the numerical model showed part of the fibers removed, marked by Fig. 18 a and b (i.e., the area where the cutting angle is acute) while the most rest of the fibers in this area was well maintained because of the bending, forming the final burrs. The experimental results presented the strip-like material formed in Stage C (Seen in Fig. 18 c) was partially removed where the remained material became the burrs, resulting in a poor machined-surface quality.

It can be seen from the above comparison that the drilling process at the hole exit predicted by the proposed FE model has been recognized to be consistent with the experimental results. The cutting of the fiber and matrix phases by the drill bit and interactions of these two phases in the drilling of the CFRPs were successfully numerically modeled by the FE model developed in this work. Therefore, it well solves the experimental limitation that is barely possible to measure such damage formation for their mechanism analysis. With the help of the FE model, the evolution process from the failure of the fiber and matrix phases at the microscale towards the macroscale burr initiation and growth in the typical CFRP drilling was well captured and the burr formation mechanism was therefore clarified under the guidance of the reliable FE modeling process. During the drilling of the CFRPs, the primary cutting edges and the flank faces of the drill bit have strongly squeezed the fiber and matrix phases at the hole exit. In this situation, the matrix was removed due to their low strength. Reversely, the fibers were deformed under the push of the drill, and the out-of-plane deformation prevented them from being removed. With the feed of the tool, the length of the fibers became longer, and they bent with the rotation of the

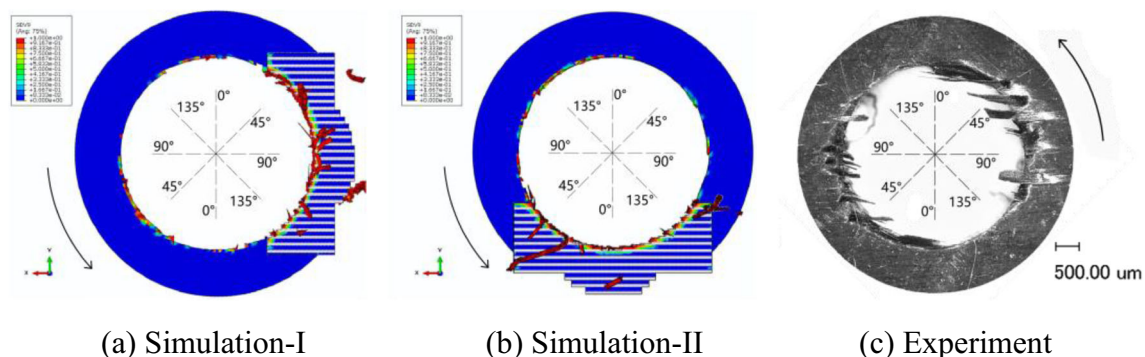
**Fig. 13** The hole exit: **a** simulation-I, **b** simulation-II, **c** experiment

Fig. 14 Twist drill and its drilling process at the hole exit

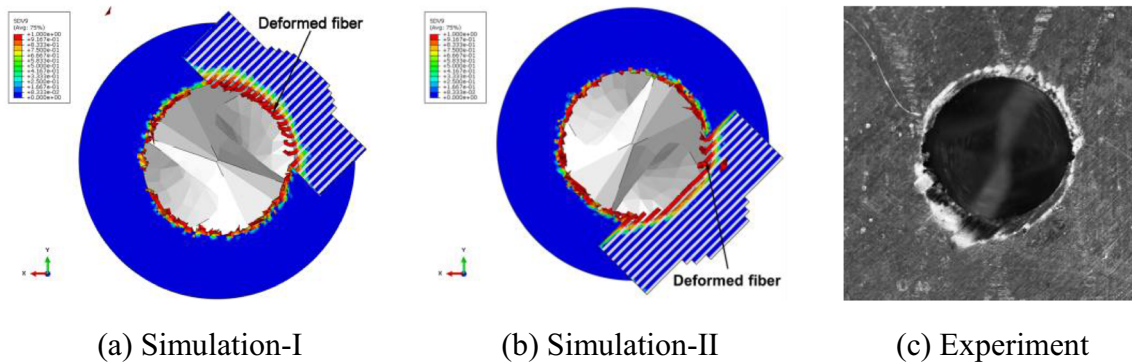
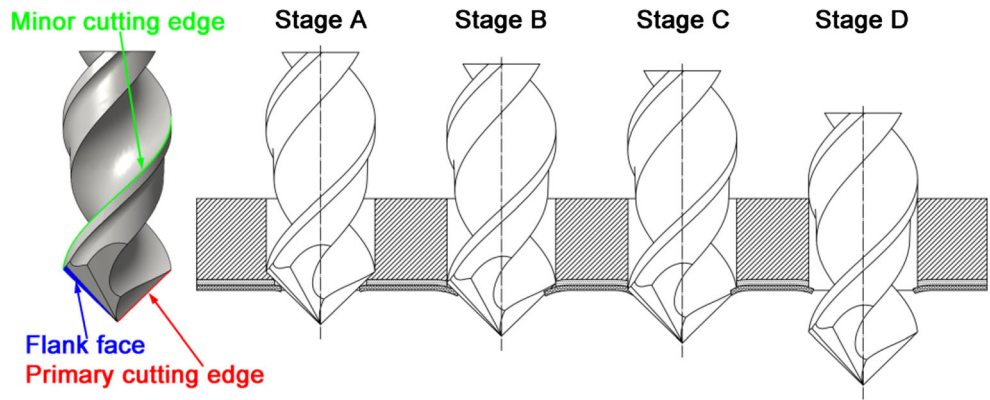


Fig. 15 The hole exit in Stage A: **a** simulation-I, **b** simulation-II, **c** experiment

drill. That could be attributed in the fibers in the area where the cutting angle was obtuse bent inward the hole radially under the push of the cutting edges, while that in the area where the cutting angle was acute bent outward the hole radially. In this case, the stress of the fibers of the latter part (i.e., the fibers in the area where the cutting angle is acute) was far to reach the ultimate strength; therefore, these fibers could not be effectively removed and the burrs were formed eventually.

#### 4.4 Computational efficiency

In addition to the identification of burrs formation, the proposed modeling has significantly improved the computational

efficiency as the additional benefit for solving the barrier of numerical modeling. Table 6 shows the calculation time of the existing drilling simulation models and the model developed in this study. It can be seen that the model developed in this study spent the shortest calculation time under relatively poor computer configuration and computing power. Obviously, the developed strategies for improve computational efficiency are effective. In particular, the strategy that dividing the cutting of fiber and matrix phases under different cutting angles into two simulations for parallel computation not only reduced the element quantities in simulation-I and simulation-II thus reduced the calculation time, and also made these two simulations calculated simultaneously thus improved the calculation efficiency.

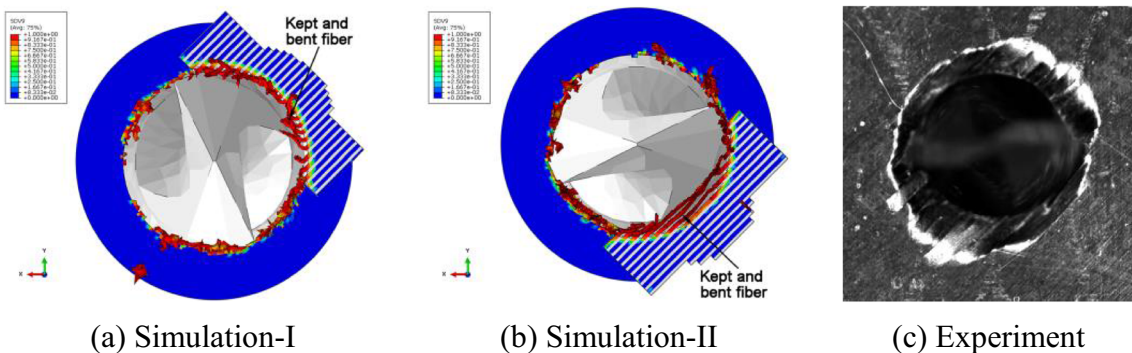
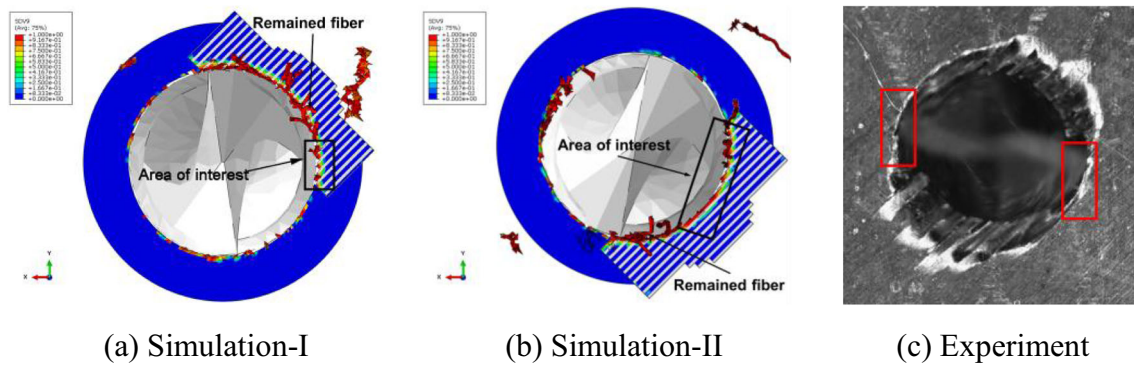
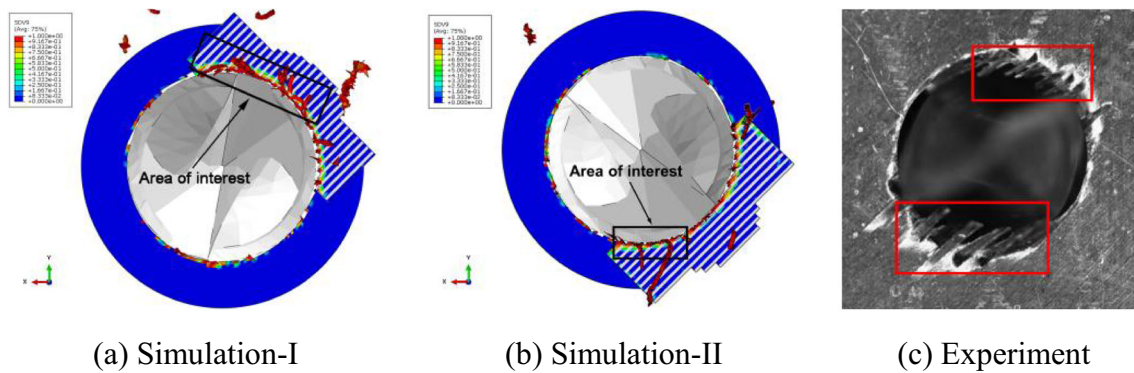


Fig. 16 The hole exit in Stage B: **a** simulation-I, **b** simulation-II, **c** experiment



**Fig. 17** The hole exit in Stage C: **a** simulation-I, **b** simulation-II, **c** experiment



**Fig. 18** The hole exit in Stage D: **a** simulation-I, **b** simulation-II, **c** experiment

## 5 Conclusions

In this paper, a three-dimensional FE model with multiscale modeling was proposed for the first time to reveal the formation mechanism of the burrs generated during the CFRP drilling. The model consists of the fiber and matrix phases and the EHM, and different material behaviors were adopted to reflect the properties of these phases. In particular, strain-based three-dimensional Hashin-type damage initiation criteria were proposed to characterize the anisotropy and difference between tensile and compressive strength of the EHM and fiber phase. Meanwhile, several methods were developed to improve the computational efficiency, and the calculation time of the model was significantly reduced. The predicted thrust force and distribution of burrs were validated via corresponding experiments, and the simulation results are in good

agreement with the experimental results. The validated FE model provides a new way to study the drilling generated burrs.

Through this FE model, the distribution of burrs at the hole exit and wall was conveniently acquired and the burr factors were calculated. It can be concluded that a lot of burrs were generated at the hole exit, while there is almost no burr at the hole wall; for the hole exit, the burrs were easily formed when the cutting angle is acute, whereas there are few burrs when the cutting angle is obtuse.

Furthermore, with this model, the cutting on the fiber and matrix phases by the drill bit and interactions of these two phases were observed, and the evolution process from the failure of the fiber and matrix phases at the microscale towards the burr formation at the macroscale was also obtained. Meanwhile, the burr formation mechanism was revealed as follows. In the CFRP drilling, the primary cutting edges and the flank faces of the drill bit have strongly squeezed the fiber and matrix phases at the hole

**Table 6** Comparison of the calculation time

References	Computer configuration	Calculation time	
Isbilir et al. [33]	8 core, 3.16 GHz CPU, 32 Gb RAM	4 months	
Phadnis et al. [36]	24 Intel quad-core, 48 GB RAM	62 h	
Feito et al. [37]	16 CPU	4 days to 3 weeks	
This study	8 core, 3.1 GHz CPU, 32 Gb RAM	Simulation-I	25 h
		Simulation-II	26 h

exit. In this situation, the matrix was removed due to their low strength. Reversely, the fibers were deformed under the push of the drill and the out-of-plane deformation hinders them from being removed. With the feed of the tool, the length of the fibers became longer, and the fibers in the area where the cutting angle was acute bent outward the hole radially. In this case, the stress of the fibers with acute cutting angle was hard to reach the ultimate strength, therefore, these fibers could not be effectively removed and the burrs were formed eventually.

The burr distribution indicates that the developed FE model has reasonably explained the formation mechanism of the burrs produced during drilling of composite. Such FE model is expected to be a useful tool to help composite engineers to minimize or even vanish the burrs and induced delamination. From the revealed mechanism, it can be concluded that the formation of burrs requires the following two conditions: firstly, the fibers at the hole exit have to be deformed out-of-plane; secondly, the deformed fibers need to be bent outward the hole radially. The former condition is the predominant to form the burrs. Therefore, it could be advised if the support could be provided under the hole or the material at the hole exit could be cut from the direction opposite to the feed direction of the drill bit, the burrs might be effectively suppressed. The latter method was deeply discussed in another study [48].

**Acknowledgments** The authors wish to thank the anonymous reviewers for their comments which lead to improvements of this paper. The authors also gratefully extend their acknowledgements to Prof. Yu Shi for his advices and contributions to the revision of the manuscript.

**Funding information** This work is financially supported by the National Natural Science Foundation of China (No. 51575082), the National Natural Science Foundation of China-United with Liaoning Province (No. U1508207), the National Key Basic Research Program of China (973 Program, No. 2014CB046503), the National Innovative Research Group (No. 51321004), Fundamental Research Funds for the Central Universities (No. DUT16TD01), and Young Scientists Fund of the National Natural Science Foundation of China (No. 51505064).

## References

- Che D, Saxena I, Han P, Guo P, Ehmann KF (2014) Machining of carbon fiber reinforced plastics/polymers: a literature review. *J Manuf Sci Eng Trans ASME* 136(34):1–22. <https://doi.org/10.1115/1.4026526>
- Abrão AM, Faria PE, Rubio JCC, Reis P, Davim JP (2007) Drilling of fiber reinforced plastics: a review. *J Mater Process Technol* 186(1–3):1–7. <https://doi.org/10.1016/j.jmatprotec.2006.11.146>
- Khashaba UA (2012) Drilling of polymer matrix composites: a review. *J Compos Mater* 47(15):1817–1832. <https://doi.org/10.1177/0021998312451609>
- Dandekar CR, Shin YC (2012) Modeling of machining of composite materials: a review. *Int J Mach Tool Manu* 57:102–121. <https://doi.org/10.1016/j.ijmactools.2012.01.006>
- Wang H, Ning FD, Hu YB, Cong WL (2018) Surface grinding of CFRP composites using rotary ultrasonic machining: a comparison of workpiece machining orientations. *Int J Adv Manuf Technol* 95(5–8):2917–2930. <https://doi.org/10.1007/s00170-017-1401-z>
- Geier N, Szalay T, Takács M (2019) Analysis of thrust force and characteristics of uncut fibres at non-conventional oriented drilling of unidirectional carbon fibre-reinforced plastic (UD-CFRP) composite laminates. *Int J Adv Manuf Technol* 100:3139–3154. <https://doi.org/10.1007/s00170-018-2895-8>
- Wang H, Cong WL, Ning FD, Hu YB (2018) A study on the effects of machining variables in surface grinding of CFRP composites using rotary ultrasonic machining. *Int J Adv Manuf Technol* 95(9–12):3651–3663. <https://doi.org/10.1007/s00170-017-1468-6>
- Azmi AI, Lin RJT, Bhattacharyya D (2012) Experimental study of machinability of GFRP composites by end milling. *Mater Manuf Process* 27(10):1045–1050. <https://doi.org/10.1080/10426914.2012.677917>
- El-Sonbaty I, Khashaba UA, Machaly T (2004) Factors affecting the machinability of GFR/epoxy composites. *Compos Struct* 63(3–4):329–338. [https://doi.org/10.1016/S0263-8223\(03\)00181-8](https://doi.org/10.1016/S0263-8223(03)00181-8)
- Faraz A, Biermann D, Weinert K (2009) Cutting edge rounding: an innovative tool wear criterion in drilling CFRP composite laminates. *Int J Mach Tool Manu* 49(15):1185–1196. <https://doi.org/10.1016/j.ijmactools.2009.08.002>
- Tan CL, Azmi AI, Muhammad N (2016) Delamination and surface roughness analyses in drilling hybrid carbon/glass composite. *Mater Manuf Process* 31(10):1366–1376. <https://doi.org/10.1080/10426914.2015.1103864>
- Wang CY, Ming WW, An QL, Chen M (2017) Machinability characteristics evolution of CFRP in a continuum of fiber orientation angles. *Mater Manuf Process* 32(9):1041–1050. <https://doi.org/10.1080/10426914.2016.1269915>
- Ning FD, Cong WL, Wang H, Hu YB, Hu ZL, Pei ZJ (2017) Surface grinding of CFRP composites with rotary ultrasonic machining: a mechanistic model on cutting force in the feed direction. *Int J Adv Manuf Technol* 92(1–4):1217–1229. <https://doi.org/10.1007/s00170-017-0149-9>
- Wang H, Ning FD, Hu YB, Li YC, Wang XL, Cong WL (2018) Edge trimming of carbon fiber-reinforced plastic composites using rotary ultrasonic machining: effects of tool orientations. *Int J Adv Manuf Technol* 98(5–8):1641–1653. <https://doi.org/10.1007/s00170-018-2355-5>
- Liu LP, Qi CL, Wu F, Xu JX, Zhu XM (2018) Experimental thrust forces and delamination analysis of GFRP laminates using candlestick drills. *Mater Manuf Process* 33(6):695–708. <https://doi.org/10.1080/10426914.2017.1376072>
- Dharan CKH, Won MS (2000) Machining parameters for an intelligent machining system for composite laminates. *Int J Mach Tool Manu* 40(3):415–426. [https://doi.org/10.1016/S0890-6955\(99\)00065-6](https://doi.org/10.1016/S0890-6955(99)00065-6)
- Iliescu D, Gehin D, Iordanoff I, Girot F, Gutiérrez ME (2010) A discrete element method for the simulation of CFRP cutting. *Compos Sci Technol* 70(1):73–80. <https://doi.org/10.1016/j.compscitech.2009.09.007>
- Jia ZY, Fu R, Wang FJ, Qian BW, He CL (2018) Temperature effects in end milling carbon fiber reinforced polymer composites. *Polym Compos* 39(2):437–447. <https://doi.org/10.1002/pc.23954>
- Wang FJ, Qian BW, Jia ZY, Fu R, Cheng D (2017) Secondary cutting edge wear of one-shot drill bit in drilling CFRP and its impact on hole quality. *Compos Struct* 178:341–352. <https://doi.org/10.1016/j.compstruct.2017.04.024>
- Bhatnagar N, Nayak D, Singh I, Chouhan H, Mahajan P (2004) Determination of machining-induced damage characteristics of fiber reinforced plastic composite laminates. *Mater Manuf Process* 19(6):1009–1023. <https://doi.org/10.1081/LMMP-200035177>
- Sheikh-Ahmad J, Urban N, Cheraghi H (2012) Machining damage in edge trimming of CFRP. *Mater Manuf Process* 27(7):802–808. <https://doi.org/10.1080/10426914.2011.648253>
- Wang FJ, Qian BW, Jia ZY, Cheng D, Fu R (2018) Effects of cooling position on tool wear reduction of secondary cutting edge

- corner of one-shot drill bit in drilling CFRP. *Int J Adv Manuf Technol* 94(9–12):4277–4287. <https://doi.org/10.1007/s00170-017-1103-6>
23. Shi Y, Pinna C, Soutis C (2014) Modelling impact damage in composite laminates: a simulation of intra- and inter-laminar cracking. *Compos Struct* 114:10–19. <https://doi.org/10.1016/j.compstruct.2014.03.052>
  24. Shi Y, Soutis C (2016) Modelling transverse matrix cracking and splitting of cross-ply composite laminates under four point bending. *Theor Appl Fract Mech* 83:73–81. <https://doi.org/10.1016/j.tafmec.2015.11.006>
  25. Zenia S, Ben Ayed L, Nouari M, Delamézière A (2015) Numerical analysis of the interaction between the cutting forces, induced cutting damage, and machining parameters of CFRP composites. *Int J Adv Manuf Technol* 78:465–480. <https://doi.org/10.1007/s00170-014-6600-2>
  26. Soldani X, Santiuste C, Muñoz-Sánchez A, Miguélez MH (2011) Influence of tool geometry and numerical parameters when modeling orthogonal cutting of LFRP composites. *Compos Part A* 42(9):1205–1216. <https://doi.org/10.1016/j.compositesa.2011.04.023>
  27. Wang FJ, Wang XN, Yang R, Gao HQ, Su YL, Bi GJ (2017) Research on the carbon fibre-reinforced plastic (CFRP) cutting mechanism using macroscopic and microscopic numerical simulations. *J Reinf Plast Compos* 36(8):555–562. <https://doi.org/10.1177/0731684416684966>
  28. Faraz A, Biermann D (2013) In situ qualitative inspection of hole exit delamination at bottom-ply during drilling of woven CFRP epoxy composite laminates. *Adv Eng Mater* 15(6):449–463. <https://doi.org/10.1002/adem.201200342>
  29. Bai Y, Jia ZY, Wang FJ, Fu R, Guo HB, Cheng D, Zhang BY (2017) Influence of drill helical direction on exit damage development in drilling carbon fiber reinforced plastic. *IOP Conf Ser Mater Sci Eng* 213:012015. <https://doi.org/10.1088/1757-899X/213/1/012015>
  30. Fu R, Jia ZY, Wang FJ, Jin Y, Sun D, Yang LJ, Cheng D (2018) Drill-exit temperature characteristics in drilling of UD and MD CFRP composites based on infrared thermography. *Int J Mach Tool Manu* 135:24–37. <https://doi.org/10.1016/j.ijmactools.2018.08.002>
  31. Shi Y, Swait T, Soutis C (2012) Modelling damage evolution in composite laminates subjected to low velocity impact. *Compos Struct* 94(9):2902–2913. <https://doi.org/10.1016/j.compstruct.2012.03.039>
  32. Santiuste C, Miguélez H, Soldani X (2011) Out-of-plane failure mechanisms in LFRP composite cutting. *Compos Struct* 93(11):2706–2713. <https://doi.org/10.1016/j.compstruct.2011.05.034>
  33. Isbilir O, Ghassemieh E (2012) Finite element analysis of drilling of carbon fibre reinforced composites. *Appl Compos Mater* 19(3–4):637–656. <https://doi.org/10.1007/s10443-011-9224-9>
  34. Isbilir O, Ghassemieh E (2013) Numerical investigation of the effects of drill geometry on drilling induced delamination of carbon fiber reinforced composites. *Compos Struct* 105:126–133. <https://doi.org/10.1016/j.compstruct.2013.04.026>
  35. Phadnis VA, Makhadmeh F, Roy A, Silberschmidt VV (2012) Drilling-induced damage in CFRP laminates: experimental and numerical analysis. *Solid State Phenom* 188:150–157. <https://doi.org/10.4028/www.scientific.net/SSP.188.150>
  36. Phadnis VA, Makhadmeh F, Roy A, Silberschmidt VV (2013) Drilling in carbon/epoxy composites: experimental investigations and finite element implementation. *Compos Part A* 47:41–51. <https://doi.org/10.1016/j.compositesa.2012.11.020>
  37. Feito N, López-Puente J, Santiuste C, Miguélez MH (2014) Numerical prediction of delamination in CFRP drilling. *Compos Struct* 108:677–683. <https://doi.org/10.1016/j.compstruct.2013.10.014>
  38. Feito N, Diaz-Álvarez J, López-Puente J, Miguélez MH (2016) Numerical analysis of the influence of tool wear and special cutting geometry when drilling woven CFRPs. *Compos Struct* 138:285–294. <https://doi.org/10.1016/j.compstruct.2015.11.065>
  39. Al-wandi S, Ding S, Mo J (2017) An approach to evaluate delamination factor when drilling carbon fiber-reinforced plastics using different drill geometries: experiment and finite element study. *Int J Adv Manuf Technol* 93:4043–4061. <https://doi.org/10.1007/s00170-017-0880-2>
  40. Calzada KA, Kapoor SG, DeVor RE, Samuel J, Srivastava AK (2012) Modeling and interpretation of fiber orientation-based failure mechanisms in machining of carbon fiber-reinforced polymer composites. *J Manuf Process* 14(2):141–149. <https://doi.org/10.1016/j.jmapro.2011.09.005>
  41. Kozey VV, Jiang H, Mehta VR, Kumar S (1995) Compressive behavior of materials: part II. High performance fibers. *J Mater Res* 10(4):1044–1061. <https://doi.org/10.1557/JMR.1995.1044>
  42. Deborah DLC (2017) Carbon composites: composites with carbon fibers, Nanofibers and nanotubes. Buffalo, New York
  43. Ueda M, Saito W, Imahori R, Kanazawa D, Jeong T (2014) Longitudinal direct compression test of a single carbon fiber in a scanning electron microscope. *Compos Part A* 67:96–101. <https://doi.org/10.1016/j.compositesa.2014.08.021>
  44. Zhou Y, Jiang D, Xia Y (2001) Tensile mechanical behavior of T300 and M40J fiber bundles at different strain rate. *J Mater Sci* 36:919–922. <https://doi.org/10.1023/A:1004803202658>
  45. Su Y (2019) Effect of the cutting speed on the cutting mechanism in machining CFRP. *Compos Struct* 220:662–676. <https://doi.org/10.1016/j.compstruct.2019.04.052>
  46. Dassault Systèmes (2015) Abaqus/CAE User's Guide
  47. Rao GVG, Mahajan P, Bhatnagar N (2007) Machining of UD-GFRP composites chip formation mechanism. *Compos Sci Technol* 67(11–12):2271–2281. <https://doi.org/10.1016/j.compscitech.2007.01.025>
  48. Jia ZY, Fu R, Niu B, Qian BW, Bai Y, Wang FJ (2016) Novel drill structure for damage reduction in drilling CFRP composites. *Int J Mach Tool Manu* 110:55–65. <https://doi.org/10.1016/j.ijmactools.2016.08.006>
  49. Hortig C, Svendsen B (2007) Simulation of chip formation during high-speed cutting. *J Mater Process Technol* 186(1–3):66–76. <https://doi.org/10.1016/j.jmatprotec.2006.12.018>
  50. Rao GVG, Mahajan P, Bhatnagar N (2007) Micro-mechanical modeling of machining of FRP composites-cutting force analysis. *Compos Sci Technol* 67(3–4):579–593. <https://doi.org/10.1016/j.compscitech.2006.08.010>
  51. Liu H, Xie W, Sun Y, Zhang J, Chen N (2018) Investigations on micro-cutting mechanism and surface quality of carbon fiber-reinforced plastic composites. *Int J Adv Manuf Technol* 94:3655–3664. <https://doi.org/10.1007/s00170-017-1110-7>
  52. Xu W, Zhang L (2017) A new approach to characterising the surface integrity of fibre-reinforced polymer composites during cutting. *Compos Part A* 103:272–282. <https://doi.org/10.1016/j.compositesa.2017.10.015>
  53. Cheng H, Gao J, Kafka OL, Zhang K, Luo B, Liu WK (2017) A micro-scale cutting model for UD CFRP composites with thermo-mechanical coupling. *Compos Sci Technol* 153:18–31. <https://doi.org/10.1016/j.compscitech.2017.09.028>
  54. Gao C, Xiao J, Xu J, Ke Y (2016) Factor analysis of machining parameters of fiber-reinforced polymer composites based on finite element simulation with experimental investigation. *Int J Adv Manuf Technol* 83:1113–1125. <https://doi.org/10.1007/s00170-015-7592-2>
  55. Yang L, Yan Y, Kuang N (2013) Experimental and numerical investigation of aramid fibre reinforced laminates subjected to low velocity impact. *Polym Test* 32(7):1163–1173. <https://doi.org/10.1016/j.polymertesting.2013.07.010>
  56. TORAY. Physical property table of Torayca yarn. <http://www.torayca.com/en/download/pdf/torayca.pdf>

**Publisher's note** Springer Nature remains neutral with regard to jurisdictional claims in published maps and institutional affiliations.